



# Phase Formation and Transformation in Alumina/YSZ Nanocomposite Coating Deposited by Suspension Plasma Spray Process

F. Tarasi, M. Medraj, A. Dolatabadi, J. Oberste-Berghaus, and C. Moreau

(Submitted July 22, 2009; in revised form August 17, 2009)

Suspension Plasma Spray process was used for deposition of pseudo-eutectic composition of alumina-yttria-stabilized zirconia as a potential thermal barrier coating using Mettech axial III torch. Process variables including feed and plasma parameters were altered to find their effects on the formation of phases in the composite coating. The in-flight particle velocity was found to be the crucial parameter on phase formation in the resulting coatings. Low particle velocities below 650 m/s result in the formation of stable phases i.e.,  $\alpha$ -alumina and tetragonal zirconia. In contrast, high particle velocities more than 750 m/s favor the metastable  $\gamma$ -alumina and cubic zirconia phases as dominant structures in as-deposited coatings. Accordingly, the plasma auxiliary gas and plasma power as influential parameters on the particle velocity were found to be reliable tools in controlling the resulting coating structure thus, the consequent properties. The noncrystalline portion of the coatings was also studied. It was revealed that upon heating, the amorphous phase prefers to crystallize into pre-existing crystalline phases in the as-deposited coating. Thus, the ultimate crystalline structure can be designed using the parameters that control the particle velocity during plasma spray coating.

**Keywords** alumina/yttria-stabilized zirconia, amorphous phase, ceramic composite coating, crystalline structure, suspension plasma spray, thermal changes

## 1. Introduction

Alumina-zirconia coatings are being considered as potential alternative to the present thermal barrier coatings (TBCs). These TBCs include cubic or tetragonal zirconia stabilized by substituting some of the Zr atoms with one or more of the base elements from alkali metal oxides such as CaO, MgO, transient metal oxides as in  $Y_2O_3$ ,  $Sc_2O_3$ ,  $Er_2O_3$  (Ref 1), rare-earths such as CeO,  $Yb_2O_3$ , or the whole Lanthanides group (Ref 2). Stabilization is to prevent the adverse effects of the phase transformation of zirconia coatings into monoclinic structure. Alternatively, stabilization can be attained in a composite with alumina, which can further enhance its thermodynamic stability at various temperatures (Ref 3), and improve its mechanical properties (Ref 4) as well as thermal resistivity (Ref 5).

F. Tarasi, M. Medraj, and A. Dolatabadi, Department of Mechanical and Industrial Engineering, S-EV 4411, Concordia University, Sir George Williams Campus, 1515 St. Catherine W., Montreal, QC, H3G 2W1, Canada; and J. Oberste-Berghaus and C. Moreau, NRC-IMI, Boucherville, QC, Canada. Contact e-mails: f\_tarasi@yahoo.com and mmedraj@encs.concordia.ca.

Both zirconia and alumina, during deposition by plasma spraying, have their own phase formation preferences. According to Golozar et al. (Ref 6), as-deposited yttria-stabilized zirconia (YSZ) coating applied by atmospheric plasma spray (APS) process shows mainly tetragonal along with some cubic structure. Alumina, on the other hand, presents the cubic  $\gamma$ -crystal structure regardless of the plasma spray technique and powder feed size (Ref 7-10). Nonetheless, some reports show that application of nanopowder feed can end up with mainly hexagonal  $\alpha$ -structure in conventional plasma spray (Ref 11).

During spray process of alumina-YSZ composite coatings, the splats may be found in at least three conditions, which include: splats formed of un-melted or partially melted feed particles, splats consisting of melted particles of either alumina or YSZ without mixing, or the blended splats composed of melted and mixed alumina-YSZ. The un-melted particles in the coating may preserve the crystalline structure of the feed materials. The melted particles of unmixed alumina or zirconia in the coatings transform into almost the same above structures, which means that zirconia in the composite coating is reported to change from mainly monoclinic to larger amounts of tetragonal and the alumina appears as  $\gamma$  or  $\delta$  (that is the transient phase before  $\alpha$ -alumina forms out of  $\gamma$ ), using APS process (Ref 12). In addition, in quench assisted APS coating the zirconia forms tetragonal along with cubic structure, while alumina is not observed in the XRD pattern (Ref 13). Liquid injection processes, on the other hand, have presented mainly tetragonal plus some cubic crystalline YSZ

and  $\gamma$ -alumina (Ref 14-17). The blended splats are strongly prone to amorphous phase formation (Ref 14, 18).

The process used in this study is suspension plasma spray (SPS) that is a kind of liquid injection process applied for deposition of very small particles ( $<5 \mu\text{m}$ ) (Ref 19). These processes employ a liquid carrier for transportation of the small solid particles into the plasma torch to circumvent the difficulty in injecting such particles. The problem with small particles is due to formation of large agglomerates which result in clogging the feed injection path. In SPS process, the feed liquid includes the suspension of the solid particles. The suspension droplets injected into the torch, undergo a sequence of fragmentation into smaller drops, evaporation of the liquid and condensation of the solid particles followed by melting. The particles with different degrees of melting, as mentioned above, will next impact the surface and form the SPS coating (Ref 20, 21).

It is expected that in every process, the spray parameters affect the above splat conditions and can be used to vary the structure of the resulting coating and may be selected for producing-specific phases. These parameters, in addition, can influence the particle velocity and temperature (Ref 22). On the other hand, the amorphous content of the composite coatings will go through crystallization process when the coating is used at high temperature. The preferred phases during this process determine the final coating structure and can consequently affect the coating properties and reliability.

The purpose of this study was: to determine the influential variables on the crystalline phase formation in SPS coatings of the pseudo-eutectic alumina-8 wt.% YSZ composite. In addition, it was to investigate the nature of transformations upon heating and the preferred crystalline structure during crystallization of the amorphous phases. Therefore, the feed material and plasma parameters in SPS process were varied to enable the prediction of the coating structure under each spray condition. The effects of heat treatment on the present phases were next studied from room temperature to  $1500^\circ\text{C}$  to investigate the

phase transformations, as well as the preferred phases during crystallization of the amorphous phase.

## 2. Experimental

A group of 16 coating samples were produced on ( $2.5 \times 2.5 \times 0.5 \text{ cm}^3$ ) mild steel coupons using SPS process. Powder feeds with weight ratio of 60 alumina/40 YSZ were deposited under various spray conditions.

To generate two different powder size ranges, first an 8 wt.% YSZ nanopowder was produced by mixing 5 wt.% YSZ and 13 wt.% YSZ powders with appropriate proportions, both with a size distribution of 30-60 nm (from Nanocomposite Powder, Inframat Advanced Materials, Farmington, CT). The resulting doped-zirconia combination was then mixed with two different sizes of alumina powders. The alumina powders were either nano with a nominal size of 27-43 nm (Nanostructured and Amorphous Materials Inc., Los Alamos, NM) or micron with an average size of  $1.4 \mu\text{m}$  (Baikowski Malakoff, Malakoff, TX). The resulting mixtures were called "Nano" and "Micron," respectively.

According to the initial assessment of the x-ray diffraction patterns of each of these powders, the zirconia feed consists of cubic structure and the alumina nanopowder contains both rhombohedral ( $\alpha$ ) and cubic ( $\gamma$ ) structure. The ratio of  $\alpha/\gamma$  in the nanopowder, according to the supplier, was of about 95/5 wt.%, while the micron-size alumina powder shows only  $\alpha$ -structure. The loose nano- and or micron-size powders after mixing were suspended in ethanol as the carrier liquid for injection of the solid feed into plasma torch. The 13 wt.% YSZ nanopowder was also deposited separately using the same process as a reference point and to investigate the preferred crystalline structure of the material without the alumina addition.

The variables studied in this work are listed in Table 1. They consist of the plasma auxiliary gas, the solid concentration in the suspension, feed rate, and the powder

**Table 1 Variables evaluated for the effect on phase formation**

Sample number	Auxiliary gas	Solid content, %	Feed rate, kg/h	Powder type	Power, kW	$V_p \pm 20$ , m/s	$T_p \pm 50$ , $^\circ\text{C}$
1	He	30	1.8	Nano	57	592	2880
2	He	30	1.8	Micron	57	605	2811
3	He	10	1.8	Micron	57	654	2600
4	He	30	1.3	Nano	56	638	3015
5	He	10	1.3	Nano	82	650	3030
6	H <sub>2</sub>	30	1.3	Micron	84	730	2780
7	He	30	1.3	Micron	81	788	2930
8	H <sub>2</sub>	30	1.3	Nano	118	810	3000
9	H <sub>2</sub>	10	1.3	Micron	117	814	2869
10	H <sub>2</sub>	30	1.8	Nano	118	815	2850
11	H <sub>2</sub>	10	1.8	Micron	116	840	2794
12	He	10	1.3	Micron	80	770	3100
13	H <sub>2</sub>	10	1.3	Nano	85	730	2995
14	H <sub>2</sub>	30	1.8	Micron	85	712	2740
15	He	10	1.8	Nano	82	790	3160
16	H <sub>2</sub>	10	1.8	Nano	85	718	2880

size range. Table 1, also, indicates the plasma powers resulted from the auxiliary gas change and variation of other spray conditions detailed in Ref 22. The variables were changed in two levels that can be extracted from the same table. It can be seen in Table 1 that the solid content have been varied from 10% to 30%, feed rate from 1.3 to 1.8 kg/h and plasma auxiliary gas has been changed from H<sub>2</sub> to He.

The resulting in-flight particle velocities and temperatures (reported in the last two columns of Table 1) at spray distance were monitored by Accura-Spray G2 (Tecnar Automation, St. Bruno, QC, Canada) diagnostic system. Since the small particle size does not allow measurements of individual particles, this system that monitors the ensemble particle velocity and temperature was used. The substrates temperatures monitored by infrared pyrometer were constantly in the range of 350-450 °C.

For structural studies, D8 Discover x-ray diffractometer (Bruker Axs Inc., Madison, WI) was used in which the XRD scanned patterns can be compared with the ICSD pattern data base. The phases were analyzed based on Reitveld refinement techniques using the Powdercell program (Ref 23).

For thermal analysis, the scanning mode of the Setaram thermal analysis machine model TG96 (SETARAM Inc., Newark, CA), was used with a heating and cooling rate of 5 °C per minute. This low rate allows better detection of all possible transformation. In this technique, the energy released or absorbed during temperature variations of the samples are measured based on the peak size.

The nature of the transformations was next verified through heat treatments of the coated samples at 700 °C for 12 h, 1000 °C for 1 h, and 1200 °C for 24 h. These temperatures were selected based on the transformation temperatures observed in the DSC graphs. In addition, heat treatment at 1500 °C for 5 h was done to determine the thermal stability of the composite at high temperatures. The heat treatments were done in air atmosphere with 200 °C per hour heating and cooling rates.

### 3. Results and Discussion

#### 3.1 Crystalline Phases

The as-deposited coatings contain different phases as shown in Fig. 1. Figure 1(a) represents the XRD pattern of the unmixed 13 wt.% YSZ powder coating without alumina that shows a fully cubic structure. Analyzing the x-ray diffraction patterns of the composite coatings revealed that stabilized zirconia, as shown in Fig. 1(a-d), basically appears as face centered cubic structure matching with ICSD database number 82-1246 with formula  $Zr_{0.8}Y_{0.2}O_{1.9}$ . The symmetry system for this structure is (225) equivalent to  $Fm-3m$  (indicated as  $t''$  structure in the database). A second compatible pattern with the XRD of the resulting coatings was the pattern number 30-1468 with formula  $Y_{0.15}Zr_{0.85}O_{1.93}$  and the same symmetry. This structure appears in both, stabilized zirconia without alumina and in its composite with alumina. There is a small

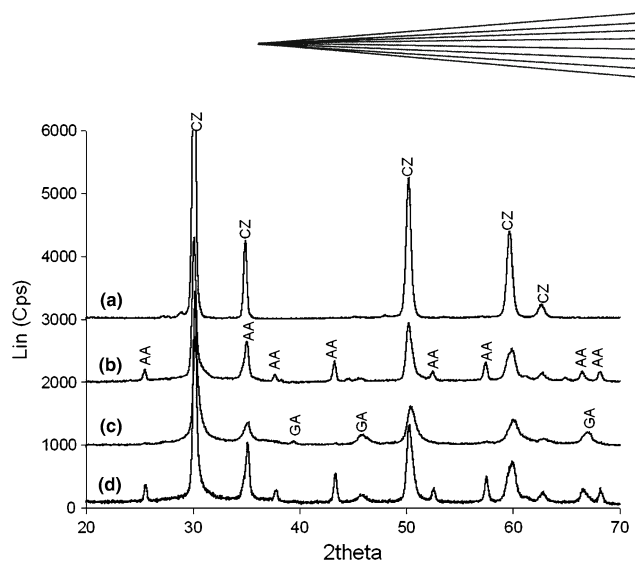


**Fig. 1** Typical XRD patterns from SPS deposition of YSZ and 60Al<sub>2</sub>O<sub>3</sub>/40YSZ under various spray conditions showing cubic zirconia (CZ) in (a) 8YSZ; (b) sample with  $\alpha$ -alumina (AA) as the major alumina phase; (c)  $\gamma$ -alumina (GA) as the major alumina phase; (d) mixture of both GA and AA alumina in addition to cubic zirconia

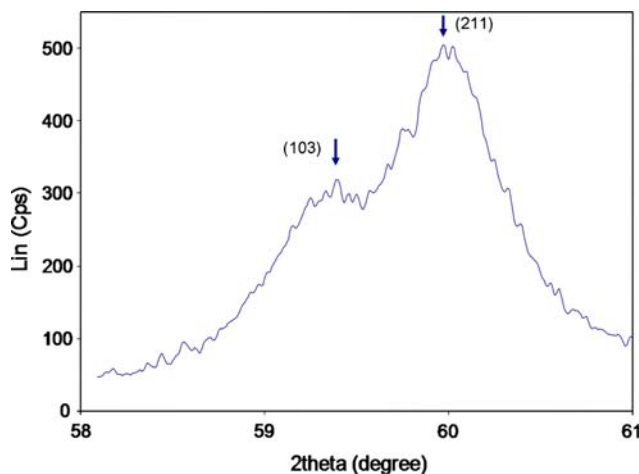


**Fig. 2** Peak splitting as an indication of tetragonal zirconia phase formation and the concerning planes to each peak

difference between the cubic and  $t''$  structure of zirconia. The difference is in the oxygen anions displacements within the structure (Ref 1) so that in  $t''$  structure there is a slight displacement from tetrahedral interstitial positions for oxygen atoms as compared with the so-called “cubic structure.” In general, the dominant structure for zirconia in this experiment was mainly cubic (or  $t''$ ) structure.

However, in a group of samples, a slight splitting of the peaks at about 59°-60° (related to the planes (103) and (211) of the tetragonal structure), as in Fig. 2, suggests the presence of some tetragonal YSZ phase. The compatible pattern for this structure in ICSD database was the pattern number 82-1242 and  $Zr_{0.88}Y_{0.12}O_{1.94}$  formula. Since the

differentiation between the cubic and tetragonal zirconia is more difficult than that between the phases of alumina, the resulting coating structures were categorized based on the alumina phases. Figure 1(b-d), respectively, represent the typical structures of the coatings in which the alumina appears in mainly cubic  $\gamma$ , mainly hexagonal  $\alpha$ , or mixed ( $\gamma + \alpha$ ) structures.

It was noticed that the samples with mainly  $\alpha$ -alumina structure (samples number 1-5 in Table 1) and the XRD pattern as in Fig. 1(b) were normally deposited using helium auxiliary gas. The  $\alpha$ -alumina with rhombohedral (hexagonal) structure is known as corundum which is identified in the database by ICSD number 71-1123, formula  $\text{Al}_2\text{O}_3$  and symmetry system (167) equivalent with R-3c. According to Table 1, this group of samples, meanwhile, is produced at low plasma powers of about 56-57 kW.

On the other hand, Fig. 1(c) represents the second group of crystal structures, consisting of cubic YSZ and  $\gamma$ -alumina. It can be seen that in most cases (samples 6 and 8-12 in Table 1), application of hydrogen auxiliary gas ensues the formation of  $\gamma$ -alumina phase with FCC structure. This structure matches with ICSD data base number 75-0921, formula  $(\text{Al}_2\text{O}_3)_{1.33}$ , and symmetry system (225) equivalent with *Fm-3m*. It can also be noticed, based on Table 1, that the majority of these samples are produced at high plasma powers (116-118 kW).

As a result, among the variables in this experiment, plasma auxiliary gas and plasma power seem to be of major influence on the phase formation in the as-deposited coatings.

It is worth to recall that plasma auxiliary gas and plasma condition (thus the plasma power) were recognized to be the most effective variables on the particle velocity, as the authors reported elsewhere (Ref 22). Consequently, these results lead to the study of the coatings crystalline phases in relation with the particle state.

The relationship between the particle temperature and velocity with the resulting crystalline phases is illustrated in Fig. 3. In this figure, the coatings with mainly  $\gamma$ -alumina are shown as round symbols and the square points are representative of the coatings with mainly  $\alpha$ -alumina. It is evident that at lower particle velocities (i.e., below 650 m/s),  $\alpha$ -alumina was formed; While at higher velocities (i.e., above 730 m/s), the dominating phase is  $\gamma$ -alumina. As an eye guide two lines are drawn in Fig. 3, to show the trend of the structural changes according to the velocity. To explain this observation, the microstructures resulting from these two particle velocity ranges were compared.

Typical SEM microstructures of the coatings at high and low particle velocities are shown in Fig. 4. It is apparent in Fig. 4(a) that higher velocities have caused wider splat spreading. This is expected because the particles with higher velocities flatten faster (Ref 24); therefore, the flattening process happens before the start of solidification (Ref 25) and the crystalline phase formation. Thin splats with large effective contact area in the inter-splat and substrate interfaces are of great importance on phase formation within the coating. It has been reported that the thermal contact resistance and splat thickness strongly affect the cooling rate (Ref 26). Thin splat with large contact area can provide rapid heat dissipation and large cooling rates. Larger cooling rates are shown to be in favor of formation of metastable phases such as  $\gamma$ -alumina (Ref 26, 27). This explanation for alumina can be generalized to zirconia splats in which more stable tetragonal phase can appear in the coatings due to lower particle velocities (lower cooling rates), while the cubic phase can occur at higher velocities (larger cooling rates) (Ref 28). Additionally, the role of unmolten or semi-molten nanoparticles entrapped in the molten particles should not be ignored. This will be discussed later in this paper.

Figure 5 presents a large in-flight solidified particle within the coating illustrating such entrapment.

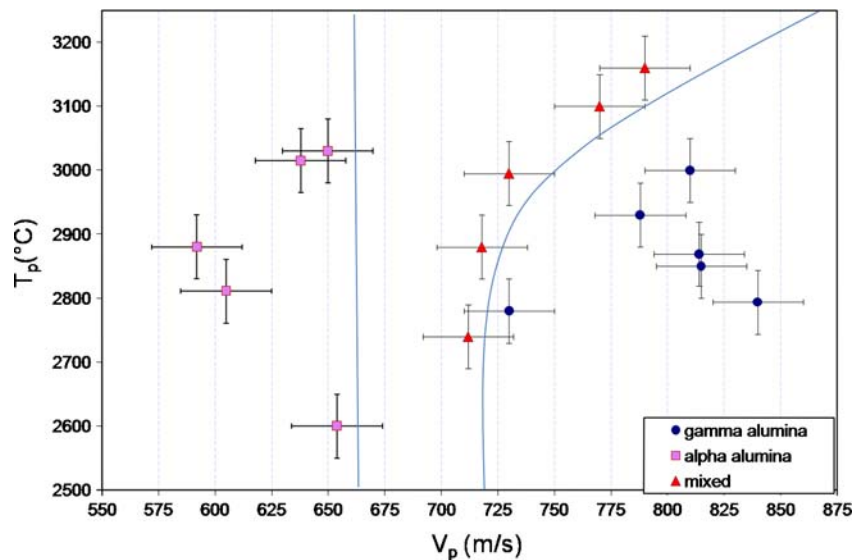
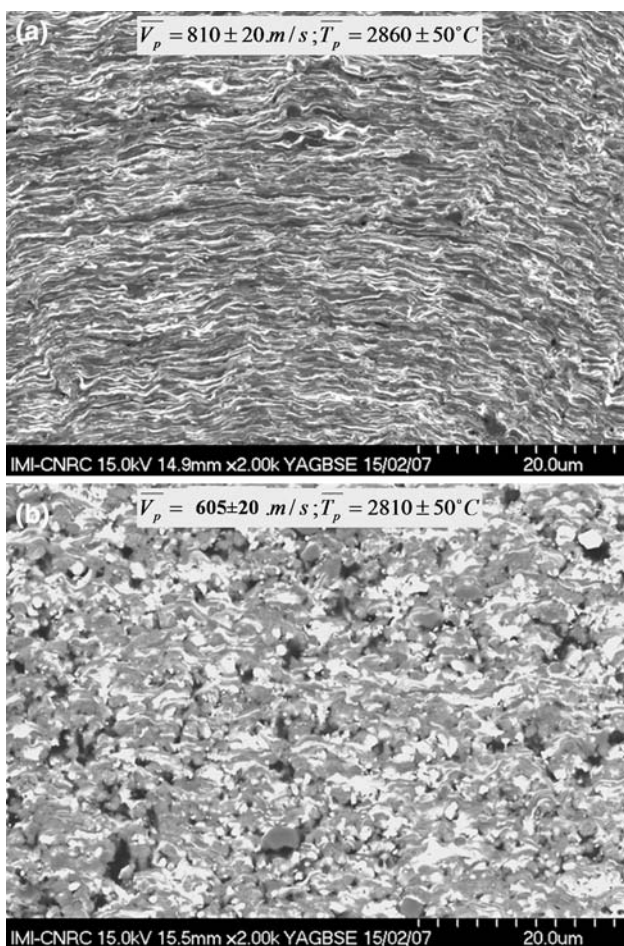
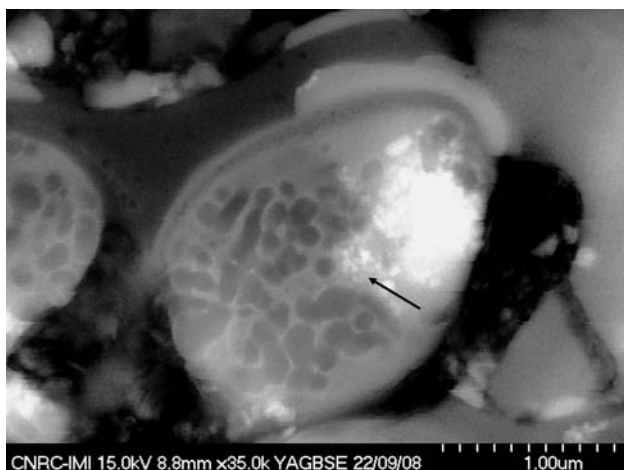


Fig. 3 Alumina component phase formation behavior within the as-deposited composite vs. the in-flight particle state



**Fig. 4** SEM micrographs of the coatings deposited using (a) hydrogen gas with high particle velocities and (b) helium auxiliary gas with lower particle velocities resulting in different splat flattening and intersplat contact area



**Fig. 5** Entrapped unmolten nanoparticles inside the large in-flight solidified particle in the coating

The clearly round edges of the particle show that it is resolidified. However, the internal particles pointed by the arrow in this figure have remained unmolten. These particles at low velocities when the in-flight solidification happens can play a pronounced role on the resulting crystalline structure. They act as the nucleation sites for the solidifying melt, so that the resultant follows the structure of these solid particles. The in-flight solidification in low velocity particles can happen due to their inability to penetrate into the resistance of the stagnating gas adjacent to the substrate. It makes these particles deflect toward tangential path almost parallel to the substrate and delay their deposition, as well as their effective impact to the surface. Therefore in a structure with a high number of in-flight solidified particles, as in Fig. 4(b), there are more chances for the formation of the initial structure of the feed powder (i.e., in this case  $\alpha$ -alumina). This fact causes more complications in prediction of the deposited coating according to the previously discussed in-flight particle state and spray condition.

Intermediate velocities, shown by triangles in Fig. 3, present a mixed structure of ( $\gamma + \alpha$ )-alumina in addition to cubic zirconia along with different amounts of tetragonal zirconia. This kind of structure can be seen in the XRD pattern of Fig. 1(d). Figure 6 indicates the relationship between the percentages of  $\gamma$ -phase in alumina compared with the cubic phase in zirconia component of the coating in these samples. This figure suggests a dependency between the present phases in the coating, indicating that the percentage of the cubic zirconia increases with increasing the  $\gamma$ -alumina content. This predicts that (metastable)  $\gamma$ -alumina coincides with (metastable) cubic zirconia formation. Thus the favorable conditions discussed for the alumina phases may be extended to the zirconia, as well. This means that the metastable cubic phases are expected at higher particle velocity (larger cooling rate).

To investigate the importance of other variables, it should be noted that the particle temperature is mainly dependent on feed parameters such as feed rate and solid

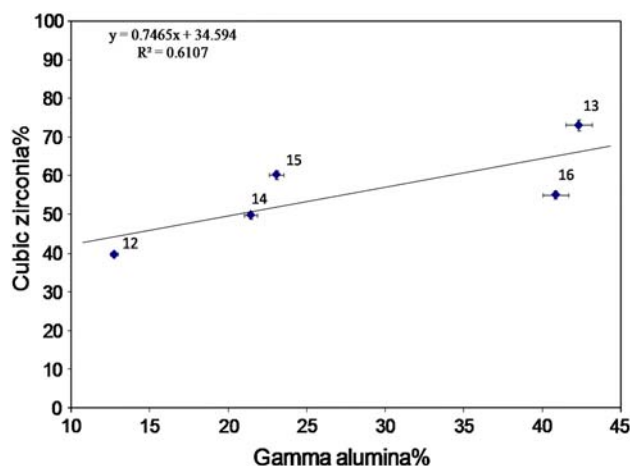


**Fig. 6** The  $\gamma$  percentage in alumina vs. the cubic phase percentage in zirconia

content (Ref 22). Therefore, these parameters can affect the structure through changing the particle temperature. The in-flight particle temperatures (in Fig. 3), are high enough for complete melting of both components (usually more than 2730 °C) and do not seem to play any major role in phase formation within the coating. The exception is that for very high particle temperatures (i.e., beyond 3000 °C, as in the last two points of the mixed structures in Fig. 3); it appears to result in formation of some  $\alpha$ -alumina phase at high velocities where domination of  $\gamma$ -phase is expected. The reason can be the impingement of overheated particles on the substrate that contributes to excessive heating of the coating and consequently the formation of  $\alpha$ -alumina phase (Ref 27). In addition, reheating the coating by the following deposition passes of the hot particles could have caused more phase transformation of metastable  $\gamma$ - to  $\alpha$ -alumina.

Although changing other variables such as particle temperature and powder size do not seem to change the type of the phases present in the coating, they may change the relative amounts of these phases. The role of these parameters, can be investigated by focusing on the coatings with mixed ( $\gamma + \alpha$ )-alumina structure and the relative amount of the metastable or stable phases.

Figure 7 shows the relationship between the  $\gamma$ -phase percentages and the particle velocity in the samples with mixed structure. In this figure, the points are indicated by the sample number corresponding to that in Table 1. To facilitate the comparisons, the particle temperature and the feed size range are included. Comparing samples 13, 14, and 16 (left side) with samples 12 and 15 (right side) in Fig. 7, verifies the effect of high temperature on phase formation. This comparison shows that very high particle temperatures in samples 12 and 15, in spite high particle velocities, have pursued almost equal or smaller amounts of  $\gamma$ -phase compared with the coatings of the lower particles velocities. Although, according to the aforementioned discussion at higher particle velocities larger metastable  $\gamma$ -phase ratios were expected. This observation confirms the previously stated role of very high particle

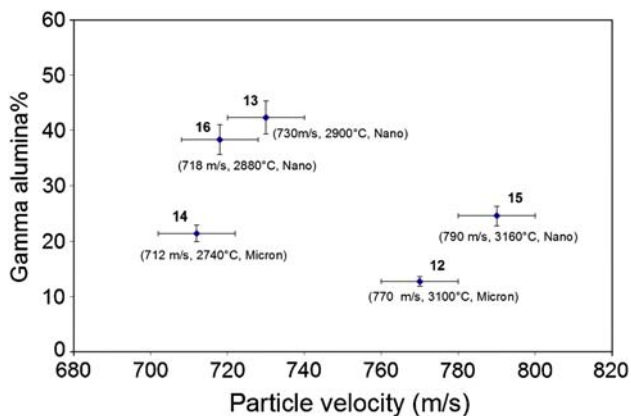


**Fig. 7** The percentage of  $\gamma$ -alumina in alumina phase vs. particle velocity in the samples with mixed structure showing the role of particle temperature and feed size range

temperatures in enhancement of more stable phases such as  $\alpha$ -alumina.

On the other hand, the minimum amounts of  $\gamma$ -alumina phase are observed in samples 12 and 14 that are the coatings from the micron-size powders. In addition, larger amount of  $\gamma$ -phase has been observed in samples 13, 15, and 16 which are produced by the nanopowder feed material. The larger particle size of alumina in the suspension of the micron powder that are expected to be surrounded by zirconia (Ref 14) end with thicker alumina splats with lower cooling rates. This facilitates the formation of more stable phases such as  $\alpha$ -alumina.

Investigation of phase changes during heating was done on a group of coating samples produced under various conditions. Regardless of processing conditions, the coatings contained a range of amounts of amorphous phase and a variety of crystalline structures, which allowed investigation of the material behavior during phase transformations.

### 3.2 Noncrystalline Phases

Other noticeable features observed in the XRD patterns of the coatings is the presence of some background humps indicative of the formation of noncrystalline phases. They appear along with wide crystalline peaks that show the very small or nanocrystalline grains. The presence of the amorphous phases was also confirmed by DSC results as will be discussed follow in the next section.

### 3.3 Thermal Analysis

The resulting curves from DSC tests are basically consisting of three major peaks exemplified in Fig. 8. The wide peak between 200 and 800 °C may be due to the relaxation phenomenon area which is characteristic of the structures containing amorphous phase (Ref 29). This relaxation involves changes in some physical properties by reduction of vacancy concentration to the equilibrium value that during rapid solidification was not possible.

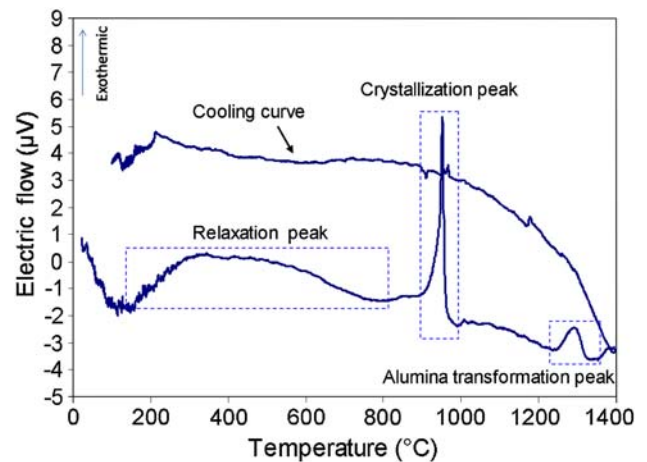


**Fig. 8** Differential scanning calorimetric (DSC) curve of a typical SPS coating showing three different peaks probable in heating process of 60Al<sub>2</sub>O<sub>3</sub>/40YSZ SPS coating

This reaction is irreversible when a glass is annealed to its glass transition temperature. Thus, the cooling curve in Fig. 8 does not show the reverse process.

However, since these peaks were sometimes observed in almost fully crystalline samples, it is expected that some additional effects should be contributing to this phenomenon. For instance, some relieving of thermal residual stresses and/or reorientation of the crystalline planes to eliminate the texture may have happened.

The second peak is sharp and related to crystallization enthalpy release at about 950 °C that is suggested to happen simultaneously from amorphous into crystalline alumina and zirconia (Ref 30). The third peak is anticipated to represent  $\gamma$  into  $\alpha$ -alumina phase transformation which takes place at around 1200 °C (Ref 7). The peak identifications can be verified by studying the heat-treated samples at 700, 1000, 1200 °C as will be explained further in this paper. However, the crystallization of certain phases from the amorphous is the matter of consideration in the following section.

### 3.4 Crystallization of the Amorphous Phase

To investigate the preferred structure during crystallization of the amorphous phases upon heating, the transformation peak areas in DSC curves were used. This helps to obtain the relative amount of each specific phase undergoing the transformation, so that the larger peak area indicates the higher amount of the phase undergoing the corresponding transformation. Therefore, the larger crystallization peak area shows the higher amorphous content and the larger  $\gamma$ - to  $\alpha$ -alumina phase transformation peak represents the larger amount of the  $\gamma$ -phase. The  $\gamma$ -phase can form during deposition process and/or as a result of crystallization of alumina out of amorphous phase during heating the DSC sample.

Figure 9 is a summary of the relation between transformation enthalpy for  $\gamma$ - to  $\alpha$ -alumina and the crystallization enthalpy that represents the amorphous content in the coatings. In these coatings, the alumina in as-deposited condition has either  $\gamma$  or  $\alpha$  structure, or mixture of both phases. This figure shows that when the as-sprayed structure contains mainly  $\gamma$ -alumina, there is a steep linear relationship between the crystallization enthalpy (the amorphous content) and the  $\gamma$  to  $\alpha$  transformation enthalpy (that represents the amount of  $\gamma$  alumina after crystallization process). This clearly indicates that increasing the amorphous content increases the amount of transformable  $\gamma$  to  $\alpha$  structure.

Conversely, when the as-deposited alumina is of mainly  $\alpha$ -structure, even at larger amorphous contents, the transformation enthalpy from  $\gamma$  to  $\alpha$  is not increasing, but it is normally almost equal to that of the crystalline samples with no amorphous phase (indicated as point A in Fig. 9 where the crystallization peak area is almost zero). This shows that in such coatings the alumina in the amorphous phase has lower tendency for crystallization into  $\gamma$ ; but it prefers to nucleate on the pre-existing  $\alpha$ -phase, so that the amount of  $\gamma$ -phase and consequently the  $\gamma$  to  $\alpha$  transformation enthalpy does not change with

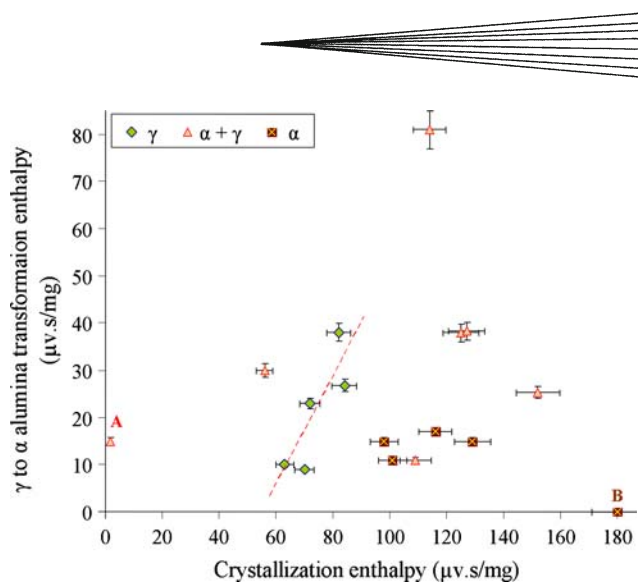


**Fig. 9**  $\gamma$ - to  $\alpha$ -alumina transformation enthalpy vs. crystallization enthalpy during heating the coatings with the crystalline alumina phase in the form of mainly  $\gamma$ , mainly  $\alpha$  or mixed structures in as-deposited condition

the amorphous content. In these coatings the tendency for crystallization on pre-existing  $\alpha$ -structure can sometimes prohibit any transformation into the  $\gamma$ -phase as can be seen in the sample assigned by point B in Fig. 9. Point B represents a coating with very large crystallization enthalpy (amorphous content) in which the  $\alpha$ -phase is the predominant structure for the alumina. In this sample, the  $\gamma$  to  $\alpha$  transformation enthalpy is zero that means during crystallization of the amorphous phase, no  $\gamma$ -alumina could have formed.

These observations suggest that the preferred phase during crystallization of the amorphous phase is dependent on the initial crystalline structures that can act as the nucleation sites for the crystallizing phases. Thus, in the coatings with mixed structure a compromise between the amounts of the two structures ( $\alpha$ - and  $\gamma$ -alumina) in the as-deposited coating is expected to determine the proportion of the resulting phases after crystallization process.

The stabilized zirconia after crystallization did not go through any further phase transformation. Thus, this sort of evaluation for zirconia component was not possible. However, the XRD pattern of the heat-treated sample, as will be discussed later, shows that the resulting structure after crystallization is not different from the crystalline YSZ initially present in the as-deposited coating.

Another noticeable observation in Fig. 9 is that the coatings with mainly  $\alpha$ -alumina structure also show a high content of amorphous phase. The reason for this concurrence must be due to the lower particle velocity that was found here to favor the formation of  $\alpha$ -alumina. The lower particle velocity results in longer dwelling time at high temperature that could provide the possibility for better mixing. The amorphous formation in a multicomponent system is influenced by the ratio of dissolution of the components. On the other hand, alumina and YSZ are almost immiscible in solid state and can mix only after melting. As a result, the lower particle velocity that causes

longer time at high temperature lead to the ideal condition for melting and mixing of the components simultaneously. This issue will be investigated further in the near future.

### 3.5 Heat Treatment

Heat-treated samples at 700 °C for 12 h show the same XRD patterns as the initial coating. The pattern also did not show any peak shift or change in grain size. This suggests that for such samples the relaxation phenomenon in the DSC curve of Fig. 8 does not involve any crystallographic phase transformation or thermal residual stress relief.

It was noticed that for most of the heat-treated coatings even at higher temperatures peak shifting did not happen. This shows the low level of the residual stress in these samples. This stress in the coatings with the microstructure as in Fig. 4(a) should have been released by extensive cracking (Ref 16). On the other hand, the microstructures such as that in Fig. 4(b) with comparatively loose and small splats do not accumulate any considerable residual stresses. Therefore, the SPS coatings of small particles do not involve any large accumulated residual stresses.

Heat treatment at 1000 °C for 1 h was carried out to investigate the crystallization phenomenon noticed in the DSC spectra. The XRD pattern of the heat-treated sample was similar to that in Fig. 10(a), consisting of cubic zirconia and  $\gamma$ -alumina. In addition, background humps of some amorphous phases were observed within the two ranges of  $2\theta$  angles, i.e., 21–40° centered at almost 31° and 42–70° centered at about 58°. Following the heat treatment at 1000 °C for 1 h, the heights of the amorphous humps were largely reduced; meanwhile the coating showed wider peaks that were more obvious in the peaks of  $\gamma$ -alumina phase as shown in Fig. 10(b). Since the primary structure formed from the amorphous phase in case of alumina (in the absence of pre-existing  $\alpha$ ) is expected to be  $\gamma$ -alumina (Ref 31), wider peaks indicate smaller average grain size as a result of crystallization of

amorphous phase into nanocrystalline structure. The quantitative investigation of the grain size according to the amorphous phase content will follow in the future.

Heat treatment at 1200 °C for 24 h results in appearing the  $\alpha$ -alumina at the expense of diminishing the  $\gamma$ -alumina peaks. This observation supports the proposed identity for the concerning peak that takes place within the range of 1200–1400 °C in DSC spectrum of Fig. 8. In contrast, in the coatings with mainly  $\alpha$ -alumina in as-deposited condition, this heat treatment did not result in any crystalline changes.

The structures of different samples after 1500 °C heat treatment for 5 h are similar and consist of  $\alpha$ -alumina and cubic zirconia. Although, sometimes the tetragonal zirconia phase is found in the samples, when pre-existing tetragonal phase was present before heat treatment, cubic zirconia phase was mostly retained and no traces of monoclinic zirconia could be found in any of the heat-treated samples. Conversely, based on the reports in  $\text{ZrO}_2$ -8 wt.%  $\text{Y}_2\text{O}_3$  coating, at 1000 °C the depletion of yttrium from zirconia unit cells has already started and at 1400 °C after 24 h about 35% monoclinic zirconia was formed (Ref 32). This indicates the considerable stability of this composite compared with conventional YSZ and its ability to prevent the transformation to monoclinic zirconia which is a major concern in TBCs performance.

It is also worth noting that coating samples upon heat treatment showed crack development that was more pronounced after high temperature heat treatments (1200 and 1500 °C). It can be mainly due to the  $\gamma$ - to  $\alpha$ -alumina phase transformation that involves about 9% shrinkage in volume (Ref 7). Crack formation at low temperature heat treatments (700, 1000 °C) can be related to the substrate/coating expansion mismatch.

## 4. Conclusion

In this work, the particle velocity is found as a crucial parameter dictating the crystalline structure of the resulting coatings. Particle velocity can be controlled by plasma parameters such as, plasma gas type and the plasma condition that in turn, determines the plasma power.

Particle temperature, as long as it is high enough for complete melting of the particles, does not play an explicit role in the type of phases. It, however, can affect the phase contents when raised far beyond the melting points of the components. Feed size also can affect the phase contents, so that the larger particles result in formation of more stable phases in the coating. Other feed parameters including feed rate and solid content influence the results through variation of the particle temperature.

The presence of unmolten nanoparticles increases the intricacy of the phase prediction in as-deposited coating.

Thermal evolution of the combined crystalline/amorphous structure of the composite coating results in crystallization of the amorphous phases as dictated by the

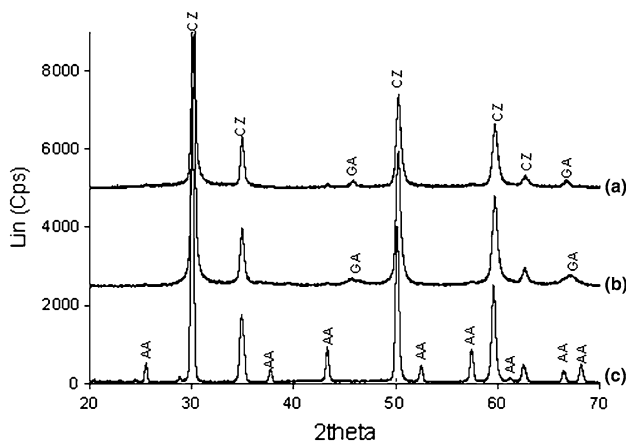


**Fig. 10** The effect of heat treatment on, (a) as-sprayed alumina—YSZ coating, (b) heat-treated coating at 1000 °C/1 h, and (c) heat-treated at 1200 °C/24 h





pre-existing structures in the as-deposited coatings. Thus, the in-flight particle velocity can also play a significant role on the final coating structure after crystallization, as it determines the initial phases in the as-deposited state.

Heat treatment at the alumina transformation temperature (1200 °C for 24 h) leads to a coating composed of mainly  $\alpha$ -alumina phase in addition to the cubic zirconia.

The crystallized structure seems to form smaller nanograins than what could be produced during plasma spray deposition. This observation needs more detailed investigation in a future work.

## Acknowledgment

Financial support from the Natural Sciences and Engineering Research Council of Canada (NSERC) is gratefully acknowledged.

## References

1. M. Yashima, M. Kakihana, and M. Yoshimura, Metastable-Stable Phase Diagrams in the Zirconia-Containing Systems Utilized in Solid-Oxide Fuel Cell Application, *Solid State Ionics*, 1996, **86-88**, p 1131-1149
2. C.G. Levi, Emerging Materials and Processes for Thermal Barrier Systems, *Curr. Opin. Solid State Mater. Sci.*, 2004, **8**(1), p 77-91
3. M. Andritschky, I. Cunha, and P. Alpuim, Thermal Stability of Zirconia/Alumina Thin Coatings Produced by Magnetron Sputtering, *Surf. Coat. Technol.*, 1997, **94-95**(1-3), p 144-148
4. A.M. Limarga, S. Widjaja, and T.H. Yip, Mechanical Properties and Oxidation Resistance of Plasma-Sprayed Multilayered  $\text{Al}_2\text{O}_3/\text{ZrO}_2$  Thermal Barrier Coatings, *Surf. Coat. Technol.*, 2005, **197**(1), p 93-102
5. P. Ramaswamy, S. Seetharamu, K.B.R. Varma, and K.J. Rao,  $\text{Al}_2\text{O}_3/\text{ZrO}_2$  Composite Coatings for Thermal-Barrier Applications, *Compos. Sci. Technol.*, 1997, **57**(1), p 81-89
6. M.A. Golozar, J. Mostaghimi, T.W. Coyle, and R. Soltani, Wear Behavior of Nanostructured and Conventional Y-PSZ Coatings, *Materials Degradation: Innovation, Inspection, Control and Rehabilitation, Proceedings of the International Symposium on Materials Degradation: Innovation, Inspection, Control and Rehabilitation*, August 21-24, 2005 (Calgary, AB, Canada), 2005, p 273-285
7. R.J. Damani and P. Makroczy, Heat Treatment Induced Phase and Microstructural Development in Bulk Plasma Sprayed Alumina, *J. Eur. Ceram. Soc.*, 2000, **20**(7), p 867-888
8. K.S. Ravichandran, K. An, R.E. Dutton, and S.L. Semiatin, Thermal Conductivity of Plasma-Sprayed Monolithic and Multilayer Coatings of Alumina and Ytria-Stabilized Zirconia, *Am. Ceram. Soc.*, 1999, **82**(3), p 673-682
9. E.T. Strangman and D. Raybould, Durable Thermal Barrier Coatings, U.S. Patent 2006/0115660, 2006
10. Z. Chen, R.W. Trice, M. Besser, Xiaoyun Yang, and D. Sordelet, Air-Plasma Spraying Colloidal Solutions of Nanosized Ceramic Powders, *J. Mater. Sci.*, 2004, **39**(1), p 4171-4178
11. Y. Zeng, C. Ding, and S. Lee, Plasma Sprayed Coatings Using Different Nano-size Alumina Powders, *Thermal Spray 2003: Advancing the Science and Applying the Technology, Proceedings of the International Thermal Spray Conference*, May 2003 (Orlando, FL, United States), 2003, p 671-674
12. X. Zhao, Y. An, J. Chen, H. Zhou, and B. Yin, Properties of  $\text{Al}_2\text{O}_3$ -40 Wt.%  $\text{ZrO}_2$  Composite Coatings from Ultra-Fine Feedstocks by Atmospheric Plasma Spraying, *Wear*, 2008, **265**(11-12), p 1642-1648
13. S. Dosta, I.G. Cano, J.R. Miguel, and J.M. Guilemany, Production and Characterization of Metastable  $\text{ZrO}_2$ - $\text{Al}_2\text{O}_3$  Coatings Obtained by APS+Quench, *J. Therm. Spray Technol.*, 2008, **17**(3), p 360-364
14. J. Oberste Berghaus, J.-G. Legoux, C. Moreau, F. Tarasi, and T. Chraska, Mechanical and Thermal Transport Properties of Suspension Thermal Sprayed Alumina-Zirconia Composite Coatings, *J. Therm. Spray Technol.*, 2008, **17**(1), p 91-104
15. A.J. Skoog, A.J. Murphy, and T.J. Tomlinson, Method for Applying a Plasma Sprayed Coating Using Liquid Injection, U.S. Patent 2006/0222777, 2006
16. A.L. Vasiliev and N.P. Padture, Coatings of Metastable Ceramics Deposited by Solution-Precursor Plasma Spray: II. Ternary  $\text{ZrO}_2$ - $\text{Y}_2\text{O}_3$ - $\text{Al}_2\text{O}_3$  System, *Acta Mater.*, 2006, **54**(18), p 4921-4928
17. A.L. Vasiliev, N.P. Padture, and X. Ma, Coatings of Metastable Ceramics Deposited by Solution-Precursor Plasma Spray: I. Binary  $\text{ZrO}_2$ - $\text{Al}_2\text{O}_3$  System, *Acta Mater.*, 2006, **54**(18), p 4913-4920
18. T. Chraska, K. Neufussa, J. Dubsy, P. Ctibor, and P. Rohan, Fabrication of Bulk Nanocrystalline Alumina-Zirconia Materials, *Ceram. Int.*, 2008, **34**(5), p 1229-1236
19. P. Fauchais, V. Rat, C. Delbos, J.F. Coudert, T. Chartier, and L. Bianchi, Understanding of Suspension DC Plasma Spraying of Finely Structured Coatings for SOFC, *IEEE Trans. Plasma Sci.*, 2005, **33**(2 Pt 3), p 920-930
20. P. Fauchais, R. Etchart-Salas, V. Rat, J.F. Coudert, N. Caron, and K. Wittmann-Teneze, Parameters Controlling Liquid Plasma Spraying: Solution, Sols, or Suspensions, *J. Therm. Spray Technol.*, 2008, **17**(1), p 31-57
21. C. Delbos, J. Fazilleau, V. Rat, J.F. Coudert, P. Fauchais, and B. Pateyron, Phenomena Involved in Suspension Plasma Spraying. Part 2: Zirconia Particle Treatment and Coating Formation, *Plasma Chem. Plasma Process.*, **26**, 2006, p 393-414
22. F. Tarasi, M. Medraj, A. Dolatabadi, J. Oberste-Berghaus, and C. Moreau, Effective Parameters in Axial Injection Suspension Plasma Spray Process of Alumina-Zirconia Ceramics, *J. Therm. Spray Technol.*, 2008, **17**(5-6), p 685-691
23. W. Kraus and G. Nolze, PowderCell, Version 2.4, Programm zur Manipulation von Kristallstrukturen und Berechnung der Röntgenpulverdiffraktogramme, Bundesanstalt für Materialforschung und -prüfung, D-12205, Berlin
24. H. Zhang, X.Y. Wang, L.L. Zheng, and S. Sampath, Numerical Simulation of Nucleation, Solidification, and Microstructure Formation in Thermal Spraying, *Int. J. Heat Mass Trans.*, 2004, **47**, p 2191-2203
25. A. Haddadi, F. Nardou, P. Fauchais, A. Grinaud, and A.C. Leger, Influence of Substrate and Coating Temperature on Columnar Growth within Plasma Sprayed Zirconia and Alumina Coatings, *United Forum for Scientific and Technological Advances*, C.C. Berndt, Ed., ASM International, 1997, p 671-680
26. P. Fauchais, M. Vardelle, A. Vardelle, L. Bianchi, and A.C. Leger, Parameters Controlling the Generation and Properties of Plasma Spray Zirconia Coatings, *Plasma Chem. Plasma Process.*, 1996, **16**(1), p 99S-125S
27. A. Vardelle, C. Robert, G.X. Wang, and S. Sampath, Analysis of Nucleation, Phase Selection and Rapid Solidification of an Alumina Splat, *Thermal Spray: A United Forum for Science and Technological Advances*, C.C. Berndt, Ed., ASM International, 1997, p 635-643
28. T. Chraska and H.K. Alexander, Transmission Electron Microscopy Study of Rapid Solidification of Plasma Sprayed Zirconia-Part II. Interfaces and Subsequent Splat Solidification, *Thin Solid Films*, 2001, **397**, p 40-48
29. J.W. Christian, *The Theory of Transformations in Metals and Alloys*, Elsevier Science Ltd./Pergamon, Oxford, 2002
30. H.-J. Kim and Y.J. Kim, Amorphous Phase Formation of the Pseudo-Binary  $\text{Al}_2\text{O}_3$ - $\text{ZrO}_2$  Alloy during Plasma Spray Processing, *J. Mater. Sci.*, 1999, **34**(1), p 29-33
31. X.-L. Wu, Q. Ren, and X.-M. He, Preparation of Nanoscale High-Purity  $\alpha$ -Alumina Powders, *Key Eng. Mater.*, 2007, **336-338**, p 2051-2053
32. J. Ilavsky, J. Wallace, and J.K. Stalick, Thermal Spray Yittria-Stabilized Zirconia Phase Changes during Annealing, *J. Therm. Spray Technol.*, 2001, **10**(3), p 497-501